



ARTICLE

Seismic Analysis of Reinforced Concrete Silos under Far-Field and Near-Fault Earthquakes

Anwer H. Hussein* and Hussam K. Risan

Department of Civil Engineering, Al-Nahrain University, Baghdad, 10072, Iraq

*Corresponding Author: Anwer H. Hussein. Email: anwer.h.hussein@gmail.com

Received: 14 July 2021 Accepted: 29 December 2021

ABSTRACT

Silos are strategical structures used to stockpile various types of granular materials. They are highly vulnerable to earthquake excitation and have been frequently reported to fail at a higher rate than any other industrial structure. The seismic response of silos within the near-fault region will suffer a complex combination of loadings due to the unique characteristics of the near-fault ground motions; which are usually associated with a large amplitude pulse at the beginning of either the velocity or the displacement time histories. This study aims to numerically evaluate the seismic response of reinforced concrete cylindrical silos under near-fault ground motions (NFGM) and far-field ground motions (FFGM). The assessment investigates the impact of the slenderness ratio and the parameters' influence on the seismic behavior of reinforced concrete silos. The validity of the Eurocode provisions in the structural safety of silos will also be inspected. The nonlinear time history analysis is carried out through the finite element approach by examining four silos with different slenderness ratios. The concrete damage plasticity model is assigned to the silo wall to simulate the nonlinear behavior of concrete in the plastic zone; while, the behavior of the stored material is represented by the Drucker-Prager plastic model. The wall-granular material interaction is considered and defined by coulomb's friction theory. The results of the near-fault records reveal a growth up to 72.8% in the hoop stress and 160.4% in the vertical stress compared to the far-field earthquakes. Consequently, the seismic response of reinforced concrete silos is highly sensitive to the type of ground motion, and slender silos tend to impose greater structural demand under the NFGM. Additionally, The Eurocode-8 seismic provisions were adequate in the conventional far-field ground motions and less effective in the near-fault zone.

KEYWORDS

Silos; seismic analysis; near-fault earthquake; far-field earthquake

Nomenclature

γ	The stored material unit weight
R	Hydraulic radius
μ	Wall friction coefficient
k	Coefficient of at-rest lateral pressure
ν	Poisson's ratio of the stored material
y	Height of the stored material measured from the top
A	Cross-section area of the silo



1 Introduction

Silos are upright bins that are used to store various types of materials such as wheat, cement, sand, and coal. They are commonly built with circular cross-sections with either reinforced concrete or steel walls. International codes and guidelines generally adopt the term squat to describe silos with shallow depths and slender silos for containers with high depth to diameter ratios. However, the complex behavior of the ensiled material produces unconventional static and dynamic loads. Accordingly, the silo walls are subjected to excessive stresses as a result of asymmetrical pressure distributions in the silo during earthquake loading [1]. The unique combination of loads has raised the rate of silo failures over any other industrial structure [2]. Thus, identifying the type and amount of loads acting on any structure is a crucial step in the assessment process. Additionally, successful numerical simulation of a silo is achieved by choosing suitable parameters to represent the silo wall, the ensiled granular material, and the contact element between the silo wall and the stored material.

The well-known classical slice theory of Janssen 1895 is widely adopted by the design standards to determine the stored material's lateral pressure on silo walls [3]. Over the years many studies have confirmed its reliability to describe granular material filling pressure [4]. However, when the silo undergoes seismic excitation the wall stresses will be dramatically changed and additional non-uniformly distributed pressures will be produced in the circumferential and vertical directions. These additional pressures are not accounted for in the seismic codes, and the seismic effect on the silo system is usually transformed to lateral static force on a cantilever beam with lumped effective masses of 80% of the total mass of the silo and its content [5,6].

However, many experimental, mathematical, and numerical studies have discussed the reliability and the cost efficiency of using the lateral static force method adopted by the silo-related international specifications. Additionally, the distinction in the seismic behavior of the squat silos and the slender silos has been evaluated by comparing the produced stresses utilizing the static lateral force method. Consequently, Durmuş et al. [7] deeply discussed the critical slenderness ratio that acts as a changing value in the seismic stresses of silos. The proposed finite element model assumed a simple elastic representation of the stored material. Moreover, Butenweg et al. [8] discussed the advantages and the disadvantages of two approaches that were used to define the ground motion over a steel cylindrical silo. The first method utilizes a finite element simulation with time history analysis (time-domain) while the second procedure was done using the frequency domain with a lumped-mass method.

Saleem et al. [9] assessed by finite element approach the effectiveness of the seismic codes in designing reinforced concrete silos. An oversimplification was noticed in this study by not considering the wall-material interaction and the assumption of an empty silo condition during earthquakes. A comparison between a numerical model of a full-interaction slender steel silo and the Eurocode-8 seismic design provisions is presented [1]. The nonlinear analysis discussed the effect of wall flexibility and sub-soil contact; meanwhile, the earthquake loading was introduced to the finite element model by the acceleration time history. Moreover, a mathematical expression was implemented to predict the lateral and hoop pressures of a flat-bottomed silo exposed to sustained horizontal and vertical accelerations [10]. The seismic behavior of elevated type reinforced concrete silos was evaluated in the initial conditions [11,12] and while silo discharging [13]. Nevertheless, the silo wall rigidity is inspected for silos subjected to ground motions [14] and the response of the ensiled material under earthquakes [15]. Furthermore, a study was implemented to discuss the causes of the major failures in singular silos [16] and a group of silos under seismic excitation [17].

This study focuses on the evaluation of the nonlinear seismic behavior of flat-bottomed reinforced concrete cylindrical silos under near-fault ground motions (NFGM) and far-field ground motions (FFGM). Though there is no fixed distance for the designation of the near-fault earthquakes; a distance range of (15–50) km is widely adopted by researchers and international codes as a reasonable value [18]. Zhou et al. [19] studied the impact of NFGM characteristics on the structural demand of structures through attention relationships for 34 near-fault records. A single degree of freedom (SDOF) system was adopted and the effect of earthquake stochastic pulse was investigated. However, ground motions that

happen within a short distance from the earthquake source often have a distinguishable characteristic when compared to those that occur at a relatively far distance. Mainly, large pulses with relatively high amplitude appear at the beginning of the earthquake records. Normally, these pulses can be recognized within the acceleration, velocity, and displacement time histories. Though, some records of the acceleration time histories may not be quite sharp catching up with such pulses [20–22], Hence, distance and Magnitude are not the only contributors to the severity of an earthquake; the direction of the fault rupture propagation concerning site location plays a critical role in deciding the earthquake intensity. This phenomenon is commonly referred to as the directivity effect of the near-fault ground motions. As a result, three types of direction effects are recognized; the forward directivity effect and the backward directivity effect [23].

Nevertheless, researchers observed numerous other factors that characterize the NFGM and contribute to the overall seismic demand of structures, e.g., the effect of the fling step. The fling step is a permanent deformation that happened as a consequence of the movement of tectonic plates. This type of deformation takes relatively little time to be formed and comes up as a pulse which is mostly recognized at the end duration of the NFGMs displacement time histories. Typically appears as a monotonic and unidirectional pulse [24–27].

2 The Finite Element Model

The international codes and standards deal diversely with the classification of silos. For instance, the Eurocode-1 [28] introduces two approaches to differentiate silo types. The first method utilizes the silo storage capacity and the symmetric discharge impact, while the second guideline employs the height to diameter ratio. However, as far as the dynamic seismic analysis is concerned, the slenderness ratio performs a vital role in the determination of the silo seismic demand. The previously covered literature survey has confirmed that claim. Consequently, the proposed system consists of four silo models with slenderness ratios of 1, 2, 3, and 4 as shown in Fig. 1. The silo base was assumed to be fixed and each model is composed of three major components; the silo wall, the ensiled bulk-type material, and the interaction between the silo wall and the stored material.

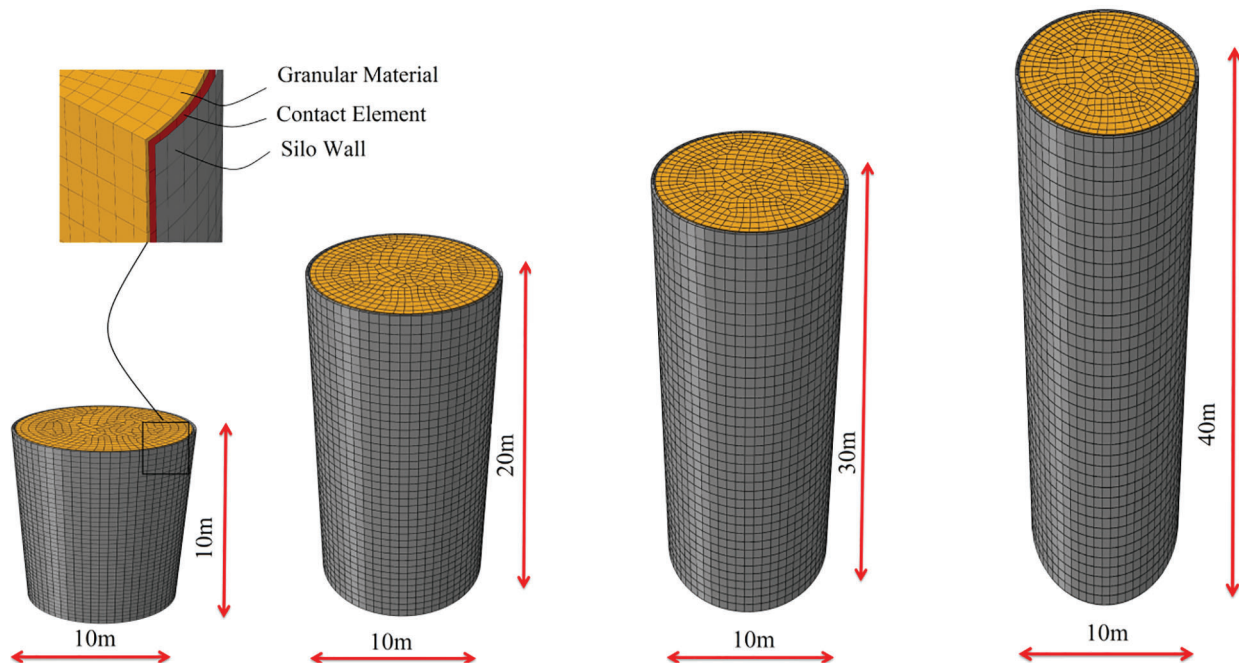


Figure 1: Silo adopted in the analysis shows different slenderness ratios

2.1 Materials Definition

A successful finite element simulation depends entirely on the proper definition of the used materials and the selection of element type. The below section characterizes the linear and nonlinear behavior of reinforced concrete wall and the ensiled granular material in addition to the criterion adopted to describe the interaction between the wall and the solids.

2.1.1 Silo Wall

4-noded doubly curved shell elements with reduced integration points (S4R) were chosen to represent the silo wall. In which, the reinforced concrete damage plasticity (CDP) model was selected to describe the nonlinear behavior of reinforced concrete walls to evaluate the tension and compression damages in the plastic regions. The mass density of concrete was set to be 2300 kg/m^3 while the Poisson's ratio (ν) was specified as 0.18. However, to obtain realistic results the parameters used to define the CDP should be properly selected and validated. Table 1 shows the values of these parameters. Concrete normally has a dilatation angle between 31° and 42° while the value of concrete viscosity is usually obtained through experiments. A detailed discussion about the selection of CDP parameters is presented by Nguyen et al. [29]. The ratio f_{bo}/f_{co} shown in the table refers to the biaxial over the uniaxial compressive strengths. The eccentricity constant and K coefficient was taken as default values suggested by the ABAQUS built-in CDM model. Further components are required to describe the compression hardening behavior as in Fig. 2a and compression damage parameter presented in Fig. 2b in addition to the tension stiffening behavior as in Fig. 2c and tension damage parameter shown in Fig. 2d.

Table 1: Concrete damage plasticity parameters

Dilation angle	Eccentricity	f_{bo}/f_{co}	K	Viscosity parameter
35	0.1	1.16	0.667	0.007985

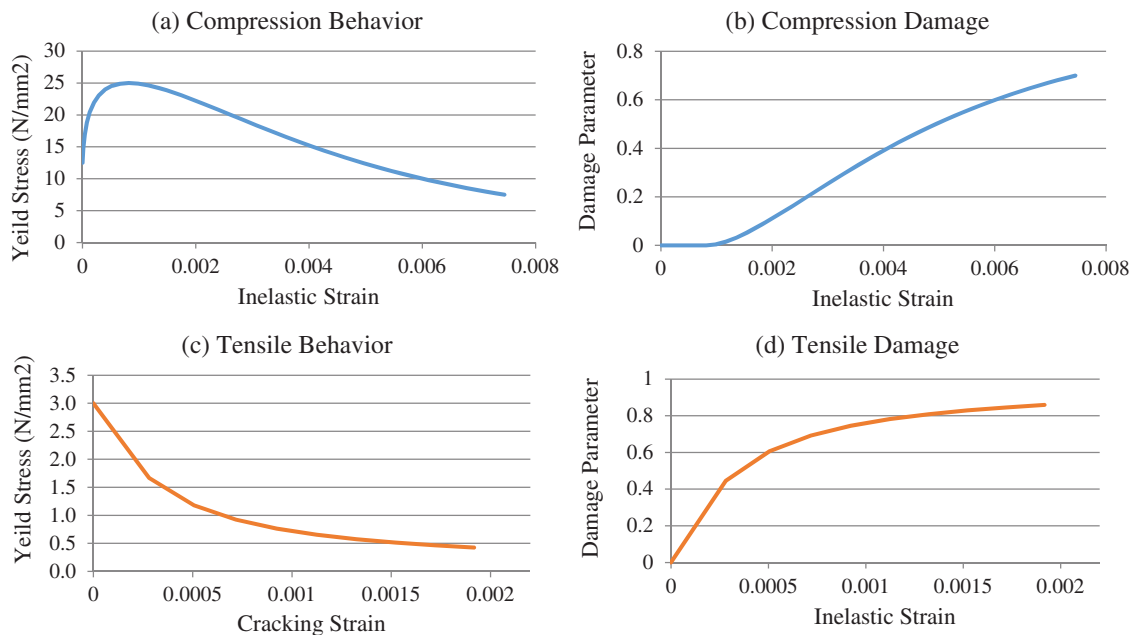


Figure 2: Concrete damage plasticity tension and compression parameters

The steel was assigned in full bond to the shell elements as double layers in the vertical and circumferential directions. The yield stress of the reinforcement bars was assumed to be 400 MPa and the ultimate stress is set equal to 600 MPa at 0.14 plastic strain. The Poisson's ratio of steel was assumed to be 0.3 and 210 GPa Modulus of Elasticity. The dimensions of silo models and their steel reinforcement are illustrated in [Table 2](#).

Table 2: Steel reinforcement of the finite element models models

Model	Height (m)	Diameter (m)	Thickness (m)	Hoop steel (Two layers)	Vertical steel (Two layers)
A	10	10	0.3	* ϕ 16 @ **S = 150 mm	ϕ 16 @ S = 300 mm
B	20	10	0.3	ϕ 20 @ S = 150 mm	ϕ 20 @ S = 250 mm
C	30	10	0.3	ϕ 25 @ S = 200 mm	ϕ 25 @ S = 250 mm
D	40	10	0.3	ϕ 25 @ S = 150 mm	ϕ 25 @ S = 150 mm

Notes: * ϕ is the diameter of the steel rebar.

**S is the center to center spacing between the steel rebars.

2.1.2 The Stored Material

The stored granular material was constructed by 8-nodes linear brick elements with reduced integration points (C3D8R) to improve numerical accuracy. The behavior of the stored material was defined both elastically and plastically. The elastic part was defined by the elastic modulus (E) of 15 MPa and Poisson's ratio (ν) of 0.3, whereas the plastic behavior was assumed to follow the Drucker-Prager constitutive plastic model. The Drucker-Prager is a perfectly plastic model that is characterized by three components; the angle of internal friction (ϕ_i), the dilation angle (ψ), and the flow stress ratio. The bulk-type material parameters are summarized in [Table 3](#), in addition to the granular material hardening explained in [Table 4](#). The Drucker-Prager parameters were adopted from previous experiments [30].

Table 3: Input parameters of the stored granular material

Parameter	Value
Density (kg/m ³)	1000
Internal friction angle (ϕ_i)	55
Dilation angle (ψ)	35
Flow stress ratio	1
Modulus of elasticity (MPa)	15
Poisson's ratio (ν)	0.3
Wall friction coefficient (μ)	0.5

Table 4: Stored material stress-strain hardening

Stress (N/m ²)	Strain
50000	0
55000	0.02
60000	0.025
70000	0.03
120000	0.035
100000	0.05

2.1.3 Wall-Granular Material Interaction

The interaction between the silo wall and the ensiled material was defined with The Coulomb friction theory. This theory is used to evaluate the friction force between the silo wall and the surface of the granular material. The friction force is the product of the force applied in the normal direction and a constant friction coefficient (μ). Two surfaces are assumed to be entirely bonded to each other. Accordingly, if the maximum friction force is achieved then the relative slipping begins. Based on the isotropic concept of the Coulomb friction criterion, the sliding between the two surfaces will occur when the resultant shear stress τ_R reaches the critical shear stress τ_{cr} . The resultant shear stress τ_R is computed from two transverse shear stress components τ_1 , and τ_2 using Eq. (1). Meanwhile, the critical shear stress τ_{cr} is the result of normal stress (σ) and constant friction coefficient (μ) as demonstrated in Eq. (2).

$$\tau_R = \sqrt{\tau_1^2 + \tau_2^2} \quad (1)$$

$$\tau_{cr} = \mu\sigma \quad (2)$$

However, a constant friction coefficient of 0.5 along the silo inner surface was assigned permitting material separation and loss of contact. ABAQUS finite element package provides a Master-Slave contact pair algorithm. In which, the silo wall was considered as a master surface since it has the larger rigidity whereas the granular material surface was set as a slave surface.

2.2 Validation of the Numerical Model

The verification process is a crucial step to maintain the accuracy and reliability of the FE computational model. Hence, the proposed three-dimensional (3D) finite element model is verified both experimentally and analytically. In the first place, the experimental work was accomplished by Wang et al. [31] employing the University of Edinburgh flat-bottomed cylindrical silo. The geometry of the validation silo was 4 m in height and 0.7 m in diameter with a 0.04 m single concentric outlet. Additionally, a total of 56 lateral pressure cells were distributed in seven levels vertically and eight layers circumferentially at 45 degrees. Fig. 3 shows the lateral pressure distribution of the validation silo.

On the other hand, the analytical verification was satisfied through Janssen's classical theory. This theory is the typical expression for the determination of the granular material pressures on silo walls and it is widely adopted by the international codes and standards. Janssen's expression is produced by solving the differential equation excreted by the vertical static equilibrium of a horizontal section of silo height. This equation can be written as follows:

$$\text{Lateral Pressure (P)} = \frac{\gamma R}{\mu} \left(1 - e^{-\frac{\mu k \gamma}{R}}\right) \quad (3)$$

where:

$$R = \frac{\text{Cross - sectional Area}}{\text{Silo perimeter}} \quad (4)$$

$$k = \frac{\nu}{1 + \nu} \quad (5)$$

The results of the normal pressure obtained from the numerical model were compared to the predictions of Janssen's expression and the experimental data and illustrated in Fig. 4. As can be seen, the results of the finite element model produce slightly higher lateral pressure than the experimental data which is acceptable, since the finite element analysis is considered a lower bound theorem. This reduces the magnitude of the calculated deformation and as result yields higher stress values. Meanwhile, the pressure of Janssen

theory and the finite model pressure are almost identical except for the extreme lower part. This difference can be attributed to Janssen’s assumptions that were assumed in the establishment of his equation. In which the friction between the stored material and the bottom of the silo is discounted which leads to the elimination of the bottom support reaction and producing uniform pressure at their intersection; in contrast to the actual case. So, the results are in a good match and the suggested finite elements model is accepted for the succeeding analysis.

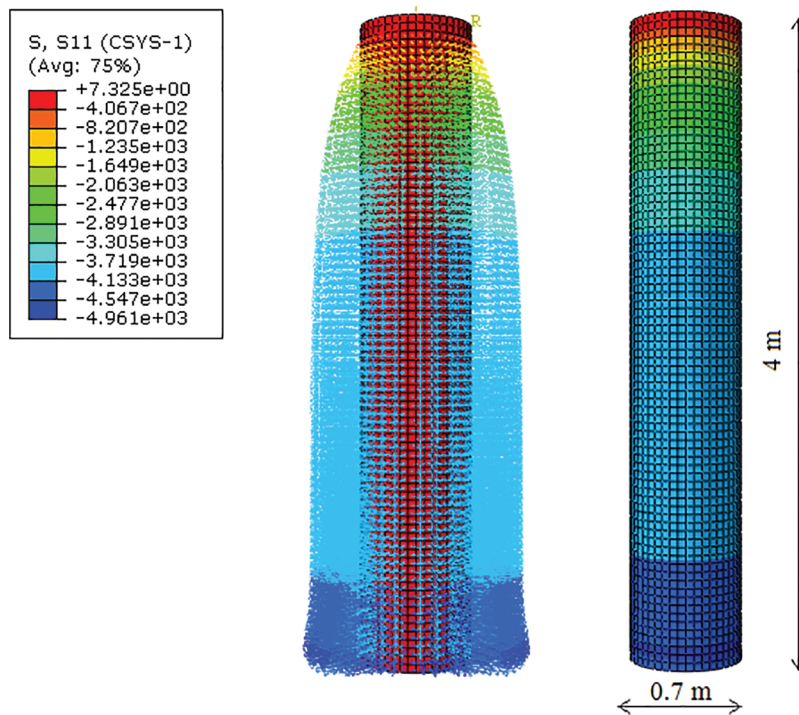


Figure 3: Lateral pressure produced by the numerical model

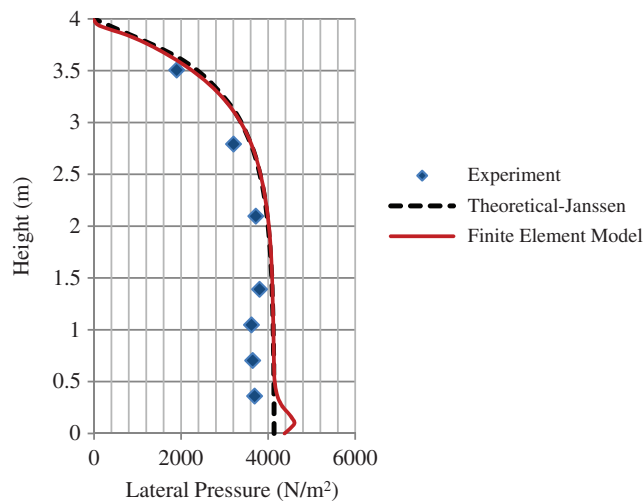


Figure 4: Validation of the Numerical model

3 Numerical Procedure

ABAQUS Finite element package with a nonlinear implicit solver was used to perform the numerical simulation. The numerical methodology was incorporated into three steps. Firstly, a free vibration eigenvalue analysis was done to extract the silo's natural frequencies. These frequencies were integrated with a damping ratio of 5% to illustrate Rayleigh factors (α , β). These factors were used to define the material inelastic damping. Secondly, the stored material was filled into the silo by introducing the gravitational forces to the system and allowing the material-wall interaction to activate the pair contact friction algorithm. The filling process is a critical step to ensure the success of the next loading stages and a total of five seconds were allocated as a time for filling and solids stabilization.

Hence, the lateral pressure at the end of the filling phase for each model was checked with the Janssen filling pressure. Lastly, the seismic excitation was implemented into the silo base. Two different time histories of the Northridge 1994 earthquake with (6.69) moment magnitude were selected. The strong motions were adopted from the Center of Pacific Earthquake Engineering Research (PEER). This center is a project established by the University of California that provides a large-scale database of crustal strong motions. The first station of (Pacoima Dam-downstr) represents the near-fault ground motion since it is located at a 7.01 km distance from the rupture. While the second station of (Riverside Airport) acts as a conventional far-field ground motion and is situated at a 98.95 km distance from the earthquake source. Additionally, to make the comparison between these two records, their peak ground accelerations (PGA) were scaled to 0.5 g. The scaled acceleration time histories of the near-fault and far-field earthquakes are illustrated in Fig. 5.

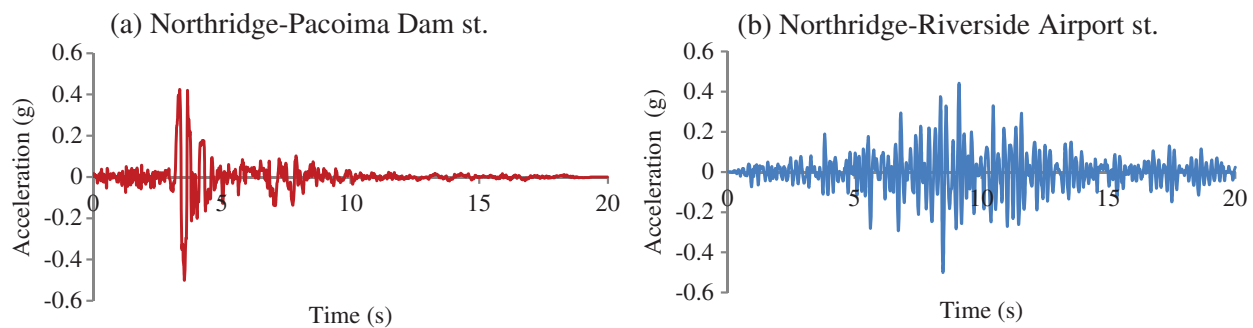


Figure 5: Scaled acceleration time histories of Northridge earthquake; (a) Near-fault St. (b) Far-field

4 Analysis Results and Discussion

The near-fault and far-field outcomes will be presented and evaluated utilizing two main categories; the first category is the overall time-based response (or massive behavior) parameters such as the base shear and the overturning moment. Meanwhile, the second category shows the precise behavior parameters along with silo depth, for instance, the hoop stress and vertical stress of the silo wall. Moreover, the effect of compression and the tension damages will be assessed for each category.

4.1 Base Shear and Overturning Moment

Silos' response to the acceleration time histories of the near-fault and far-field ground motions of the Northridge 1994 earthquake was assessed in regards to base shear and base moment time histories; in addition to the concrete tension and compression damage propagations. For each factor, the influence of four different slenderness ratios was evaluated to estimate the structural safety and to specify the critical loading case. However, a total of eight runs were demonstrated and its corresponding base shear and base moment time profiles are presented in Figs. 6–9.

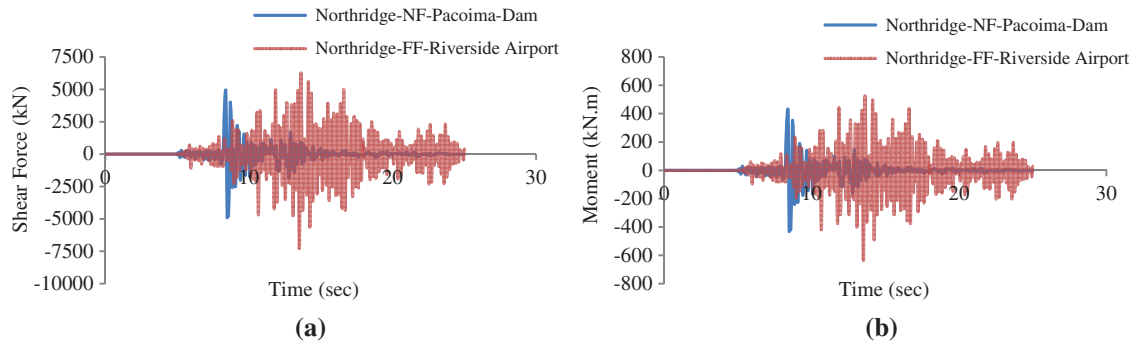


Figure 6: Model-A seismic response profiles: (a) Base shear, (b) Overturning moment

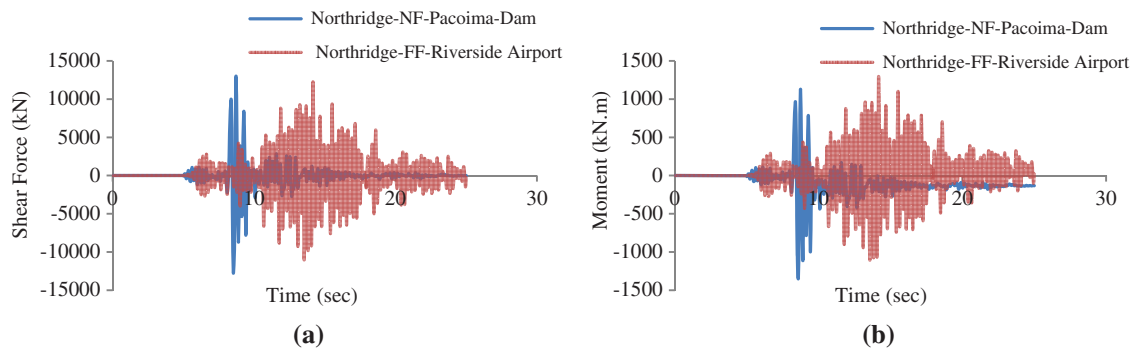


Figure 7: Model-B seismic response profiles: (a) Base shear, (b) Overturning moment

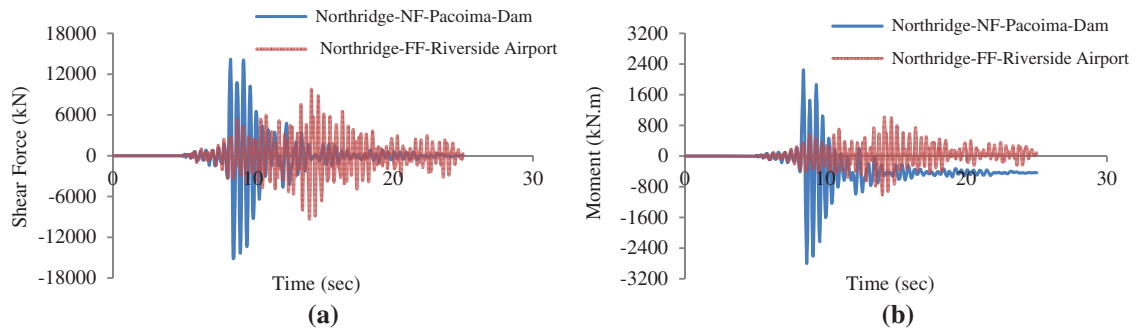


Figure 8: Model-C seismic response profiles: (a) Base shear, (b) Overturning moment

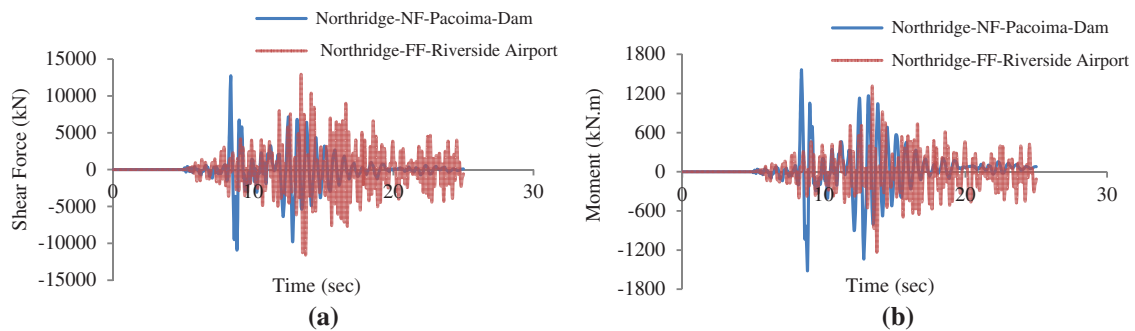


Figure 9: Model-D seismic response profiles: (a) Base shear, (b) Overturning moment

For Model-A of a squat silo with a height to diameter ratio = 1.0, the structural demand of the Riverside far-field ground motion station was higher than the Pacoima near-fault ground motion station. The percentage near-fault to far-field results of the base shear and overturning moment were 68.3% and 68.2%, respectively. While for Model-B of 2.0 slenderness ratio, the response of the near-fault station was slightly higher than the far-field station with no more than 5.8% increment in terms of maximum base shear and moment. However, a dramatic increase was recorded for Model-C with a slenderness ratio = 3.0, which has yielded the greatest demand for the NF station, with an NF/FF ratio of 155.1% maximum base shear and 274.5% in the max base moment. Finally, for model-D with an aspect ratio = 4.0 the max base shear in both NFGM and FFGM stations were almost identical, whereas the max overturning moment was 19.1% higher in the NFGM station. [Table 5](#) summarizes the results of max base shear and base moments for all models.

Table 5: Summary of the maximum base shear and maximum overturning moment

Model	Slenderness ratio	Base shear (kN)			Overturning Moment (kN·m)		
		NF	FF	*Ratio (%)	NF	FF	Ratio (%)
A	1.0	4949.0	7247.4	68.3	433.6	636.1	68.2
B	2.0	12972.3	12255.8	105.8	1351.6	1296.3	104.3
C	3.0	15157.8	9771.4	155.1	2796.9	1018.8	274.5
D	4.0	12720.0	12922.7	98.4	1563.9	1312.8	119.1

Notes: *Ratio is the percentage of the near-fault to the far-field values.

On the other hand, the impact of seismic loading on the tension and compression behavior of the reinforced concrete walls has also fluctuated. At first, the squat-type silo has not experienced any concrete damage neither in the near-fault record (Pacoima Dam St.) nor in the far-field station (Riverside Airport St.). For Model-B, tension cracks occurred and were mostly concentrated at the base part of the silo. In which the silo wall with NFGM record was damaged slightly more than the near-fault station. Unsurprisingly, Model-C endures aggressive concrete tension damage for the Pacoima near-fault station and it was spread along the lower half of the silo wall as shown in [Fig. 10](#). Additionally, [Fig. 11](#) reveals a presence of compressive crush in the lower part of Model C, whereas no other model has suffered from it. Finally, only the near-fault records caused concrete tension damage in the silo base region for Model D while the FFGM station showed no loss. Hence, for minimizing the graph's area, only Model C tension and compression results were shown.

4.2 Silo Wall Stresses

The determination of the amount and distribution of silo stresses is essential to understanding the seismic behavior of silos. Additionally, the hoop stress (f_h) and the vertical stress (f_v) are the key parameters to design the grid steel reinforcement of the silo wall. Hence, these stresses will be evaluated for the same above-mentioned four slenderness ratios (S_r). [Figs. 12–15](#) show the distribution of maximum hoop and vertical stresses for Model-A through Model-D, respectively.

As can be observed, for the squat silo of $S_r=1.0$, the far-field station response was greater than the response of the near-fault record for both stresses. This is the only case to get higher demand under FFGM than NFGM. On the other hand, the results of Model-B ($S_r=2.0$) reveal equivalent stresses for the near-fault and far-field records, and the location of the peak stresses was at the bottom quarter of the silo for all cases. Nevertheless, Model-C ($S_r=3.0$) has a remarkable performance in the near-fault record for both stresses. However, the behavior of Model-D ($S_r=4.0$) has fluctuated over the type of ground motion. In which the hoop stresses for the NFGM and FFGM have yielded comparable values, meanwhile the NFGM

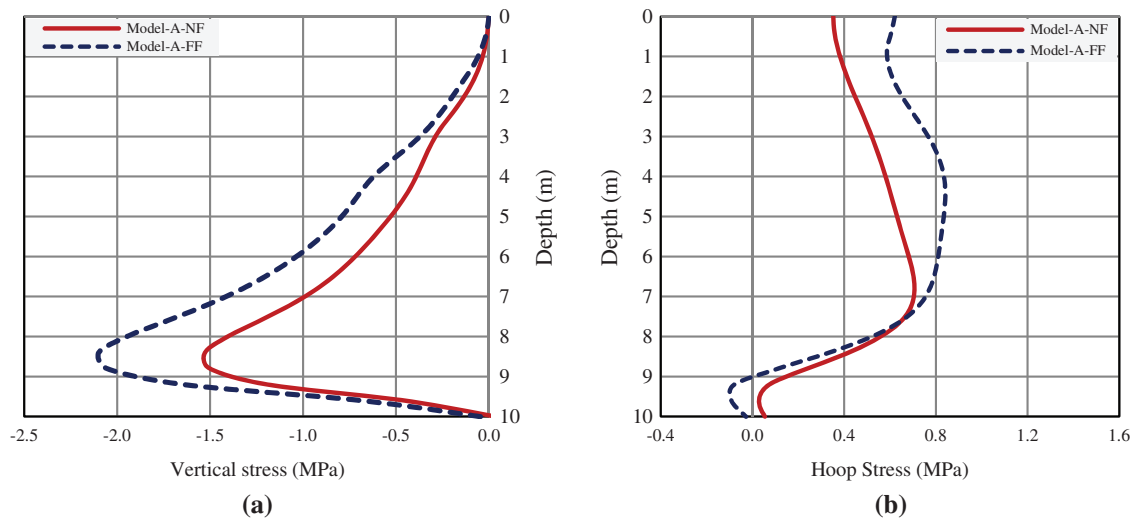


Figure 12: Model-A maximum wall stresses distribution; (a) Vertical stress, (b) Hoop stress

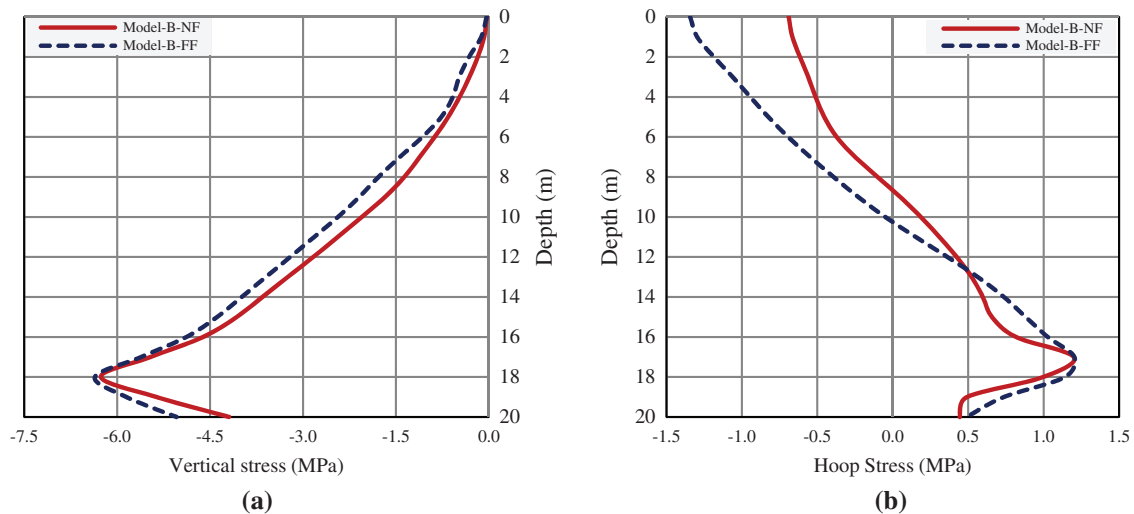


Figure 13: Model-B maximum wall stresses distribution; (a) Vertical stress, (b) Hoop stress

This distinction in the behavior of the squat-type silos and slender silos has been also noticed by previous studies [7,8]. Therefore, this judgment can be generalized for squat silos under any type of seismic excitations. On the other hand, $Sr=3.0$ is proposed by this study as a critical aspect ratio due to its outstanding seismic demand under NFGM; which amend the ratio of $Sr=2.0$ that was previously suggested by Durmuş et al. [7] for RC silos under conventional seismic excitations.

On the other hand, Table 6 summarizes the results of the maximum tensile hoop stress (f_h) and the maximum compressive vertical stress (f_v) of the four models. As can be demonstrated throughout all models, the ratios of the near-fault to the far-field results show overall compliance with the previously discussed ratios of the maximum base shear and overturning moment presented in Table 5. However, the only exception was for the near-fault results of Model-D, in which the response in terms of wall stresses was higher than the base shear and moment. Consequently, the ratio of NFGM to the FFGM was 117.7% for the maximum f_h and 233.8% for maximum f_v ; meantime the maximum base shear and maximum overturning moment have NFGM/FFGM values of 98.4% and 119.1%, respectively.

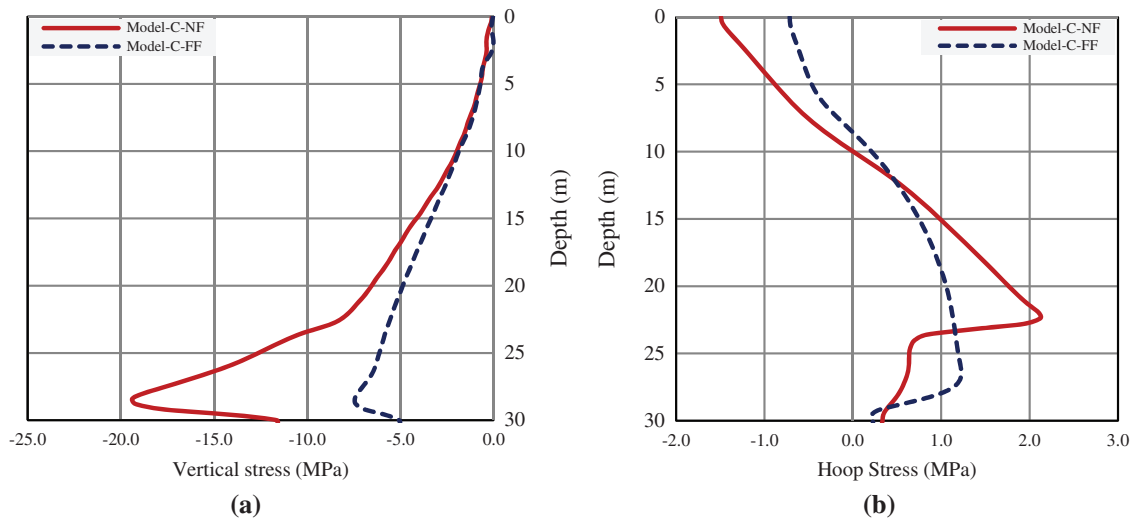


Figure 14: Model-C maximum wall stresses distribution; (a) Vertical stress, (b) Hoop stress

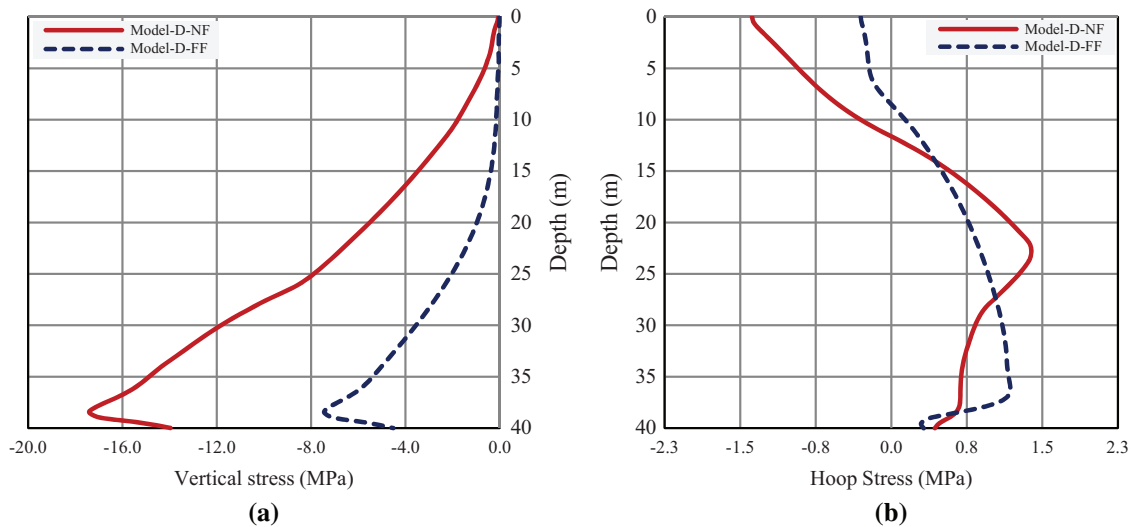


Figure 15: Model-D maximum wall stresses distribution; (a) Vertical stress, (b) Hoop stress

Finally, the tendency of the silo wall stresses in the near-fault record was climbing upward as the slenderness ratio (S_r) increased except for $S_r = 3.0$ which produced higher stresses than $S_r = 4.0$ as shown in Fig. 17. Nevertheless, the demand for far-field ground motions was moving up stably over the slenderness ratios, as illustrated in Fig. 18. It's noticed for both NFGM and FFGM that the variations of the maximum hoop stresses were less than the changes in the peak vertical stresses. This difference is mainly due to the column packing effect of solid materials which transfers a portion of the lateral pressure of solids into a friction force on the surface of the silo walls. That portion increases as the column height of solid material increases resulting in additional axial stress and impacting the hoop stress distribution. Also, it can be illustrated that the positions of the maximum hoop stresses are mostly located in the middle region of silo depth for NFGM and close to the silo base for FFGM. Consequently, the observed distribution of the maximum hoop stresses of silos under FFGM is fully consistent with the results of the preceding works [1,7,8]; which are, apparently, not valid when silos are subjected to NFGM.

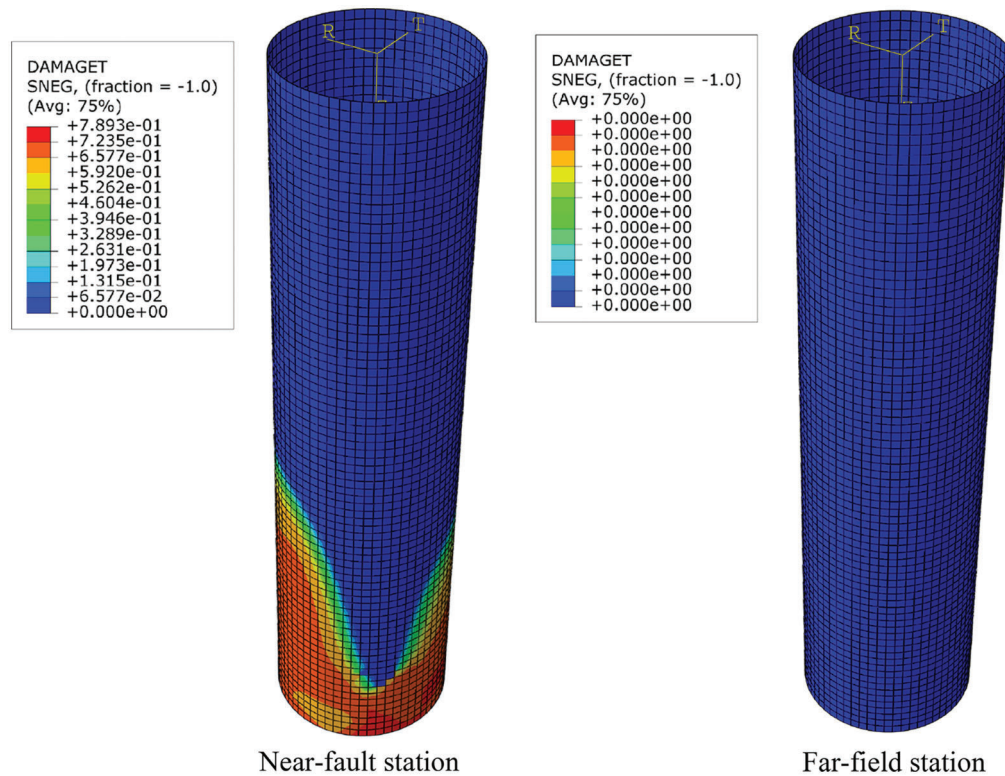


Figure 16: Model-D tension damage propagation due to Northridge earthquake

Table 6: Summary of the maximum tensile hoop stress and maximum compressive vertical stress of silo wall under near-fault and far-field ground motions

Model	Slenderness ratio	Hoop stress (Mpa)			Vertical stress (Mpa)		
		NF	FF	*Ratio (%)	NF	FF	Ratio (%)
Model-A	1.0	0.71	0.84	84.0	1.53	2.10	72.8
Model-B	2.0	1.20	1.20	99.8	6.26	6.36	98.4
Model-C	3.0	2.12	1.23	172.8	19.39	7.44	260.4
Model-D	4.0	1.39	1.18	117.7	17.41	7.45	233.8

Notes: *Ratio is the percentage of the near-fault to the far-field values.

5 Evaluation of the Seismic Codes under NFGM and FFGM

To compare the stress results of the finite element models under NFGM and FFGM, the Eurocode-8 procedure is selected as a reference for the seismic evaluation of silos. However, the response spectral acceleration will be extracted utilizing the Eurocode-1, AISC SEI 7/16, IBC-2012, UBC-97, and IS-1893/2016. Hence, these codes have been audited to obtain the code that predicts the highest stress demand. Consequently, the Eurocode-1 and AISC SEI 7/16 has yielded the highest values of the response spectral acceleration over all of the models for the selected near-fault and far-field ground motions that as shown in Fig. 5. As a result, the comparison in hoop stresses between the Eurocode-8 with Model-A ($S_r = 1.0$) and Model-B ($S_r = 2.0$) are presented in Figs. 19a and 19b, respectively. As can be seen, the Eurocode-8 procedure was able to control the demands of both ground motions. However, the Eurocode-

8 was less effective in predicting the hoop stresses of Model-C ($S_r = 3.0$) and Model-D ($S_r = 4.0$) under NFGM as cleared in Fig. 20a. Meanwhile, the hoop stresses of the FFGM were successfully estimated by the Eurocode-8 as shown in Fig. 20b. These results confirm that the seismic codes are derived from far-field earthquakes. However, the effectiveness of the Eurocode-8 in the seismic analysis of silos experiencing FFGM complies with the conclusions of [8]; whereas, the outcomes of the NFGM disagree with their suggestions.

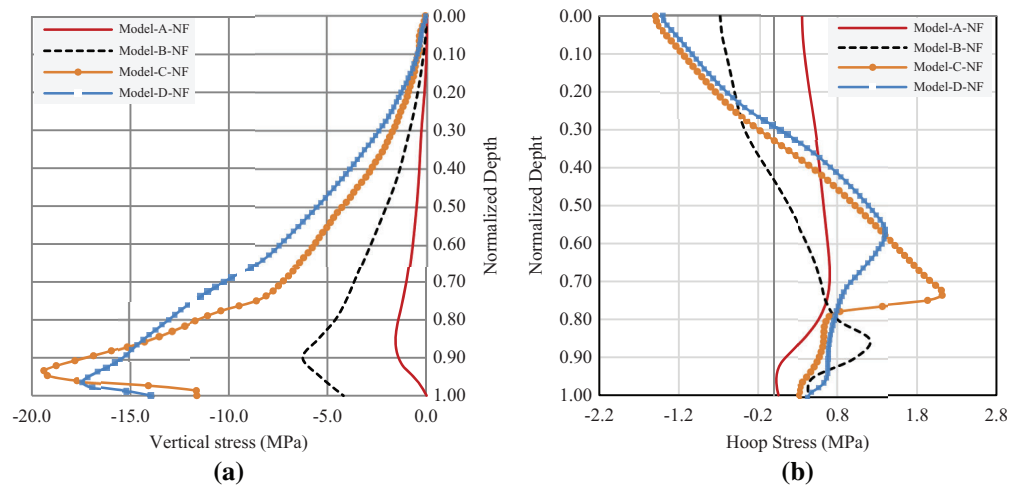


Figure 17: Maximum wall stresses distribution of the FE models under Near-fault ground motion; (a) Vertical stresses, (b) Hoop stresses

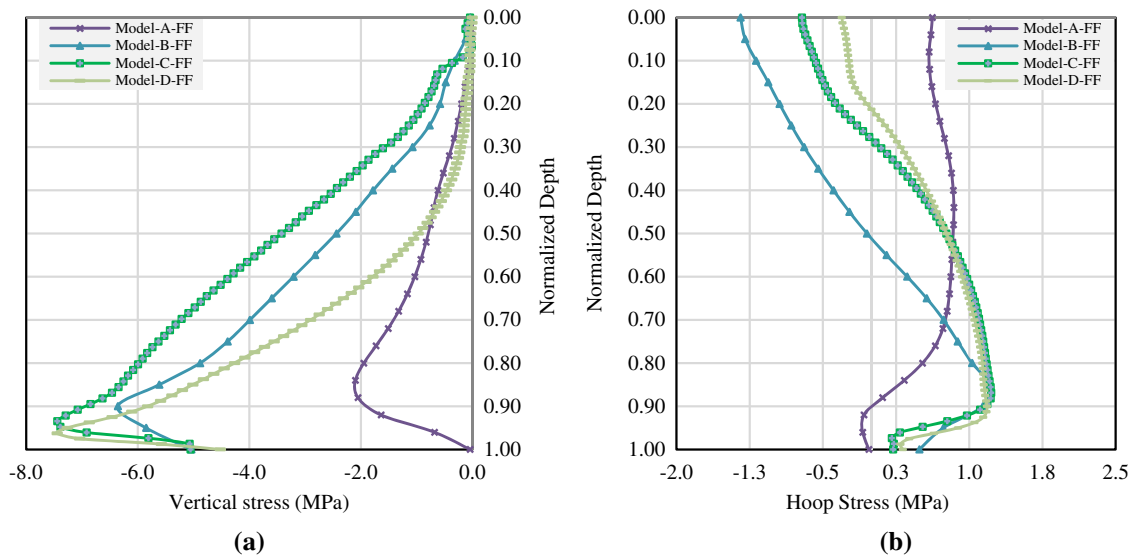


Figure 18: Maximum wall stresses distribution of the FE models under far-field record; (a) Vertical stresses, (b) Hoop stresses

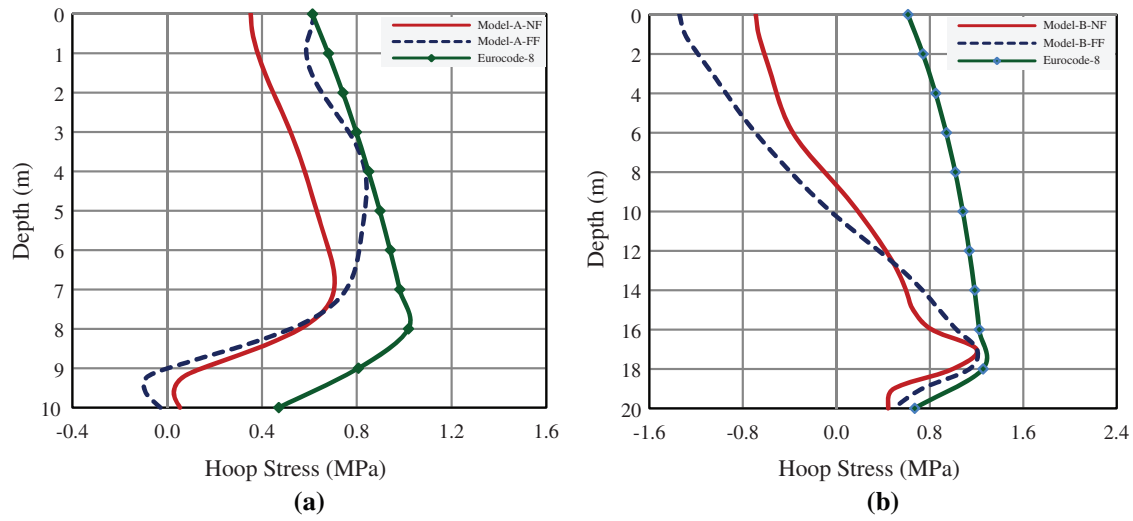


Figure 19: Comparing the hoop stresses of near-fault and far-field earthquakes with the Eurocode-8; (a) Model-A, (b) Model-B

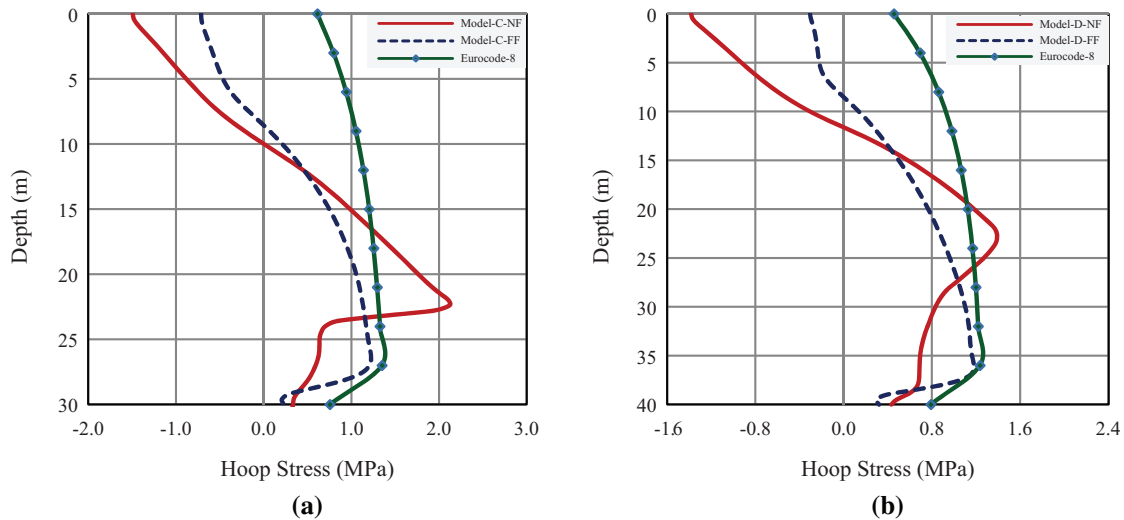


Figure 20: Comparing the hoop stresses of near-fault and far-field earthquakes with the Eurocode-8; (a) Model-C, (b) Model-D

6 Major Parameters Effect on the FE Results

The evaluation of the main input parameters will be executed utilizing a 20 m height, 10 m diameter, and 0.3 m thickness flat-bottomed reinforced concrete silo. The stored material is defined by the Drucker-Prager criterion and the interaction between the silo wall and the stored material was introduced utilizing Coulomb friction theory with constant friction of $\mu = 0.5$, allowing material separation and loss of contact. The seismic loading is defined by the acceleration time history of the Chi-Chi_TCU102 earthquake ($M_w = 7.62$, $R_{rup} = 1.49$ km, and $PGA = 0.212$ g) as shown in Fig. 21. The material damping is added using Rayleigh factors with a damping ratio $\xi = 5\%$. Hence, examining the impact of each parameter will be executed by varying its input values while other factors remain stationary. However, it is crucial to comprehend that the impact will not be the same using a different

combination of the input parameters, but it does provide a general impression of the effectiveness of the parameters.

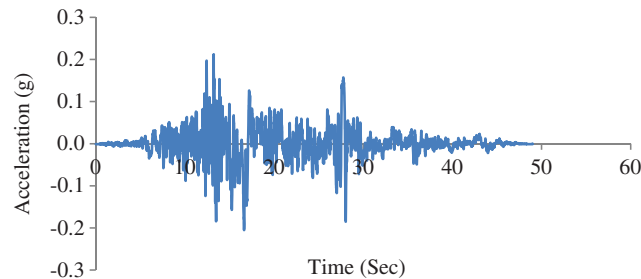


Figure 21: Acceleration time histories of Chi-Chi-Taiwan (1999) earthquake

6.1 Wall-Material Friction

The roughness between the silo wall and the stored material is a key parameter in determining the stored material pressures as has been discussed in the previous sections. The roughness herein is evaluated by the coefficient of the wall friction (μ). Therefore, three values of wall friction coefficient ($\mu = 0.2$, $\mu = 0.3$ and $\mu = 0.4$) have been investigated in terms of maximum hoop stress. As can be demonstrated from Fig. 22, the maximum hoop stress has been raised by 32.6% when the wall friction coefficient decreases from 0.6 to 0.2. This growth can be assigned to the role of the wall friction in transferring a fraction of the lateral pressure of

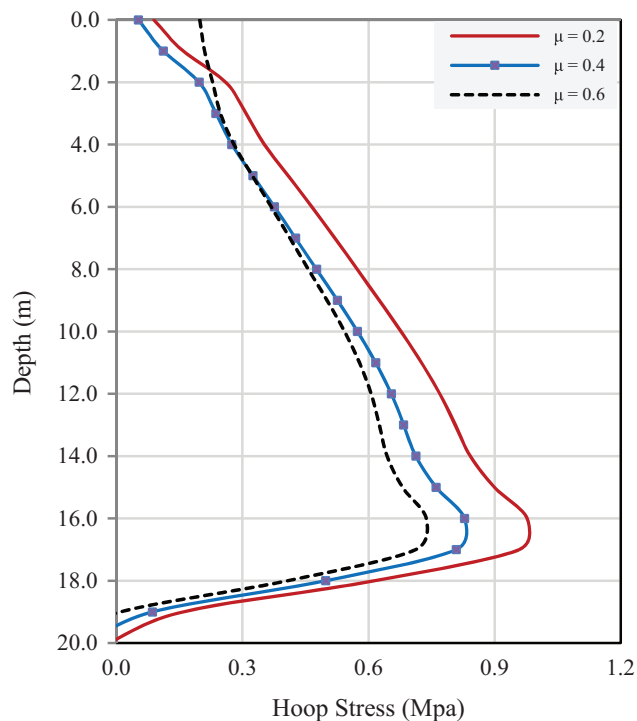


Figure 22: The effect of wall friction coefficient (μ) on the seismic hoop stress of the FE model

the stored material as a vertical compressive pressure in the silo wall. Accordingly, low values of μ will transform less lateral pressure as vertical stress and higher hoop stress in the wall of the RC silo.

6.2 Poisson's Ratio of the Stored Material

Poisson's ratio (ν) or the ratio of the lateral strain to the longitudinal strain of the stored granular material is a major contributor to the computation of the granular pressure. There is a strong relationship between the Poisson's ratio (ν) and the lateral pressure coefficient as has been previously shown in Eq. (5). However, this effect under seismic excitation is assessed by employing Poisson's ratio (ν) of $\nu = 0.2$, $\nu = 0.3$, and $\nu = 0.4$ as can be seen in Fig. 23. The result indicates an increment of 53.5% in the silo wall hoop stress when moving the Poisson's ratio (ν) from 0.2 to 0.4.

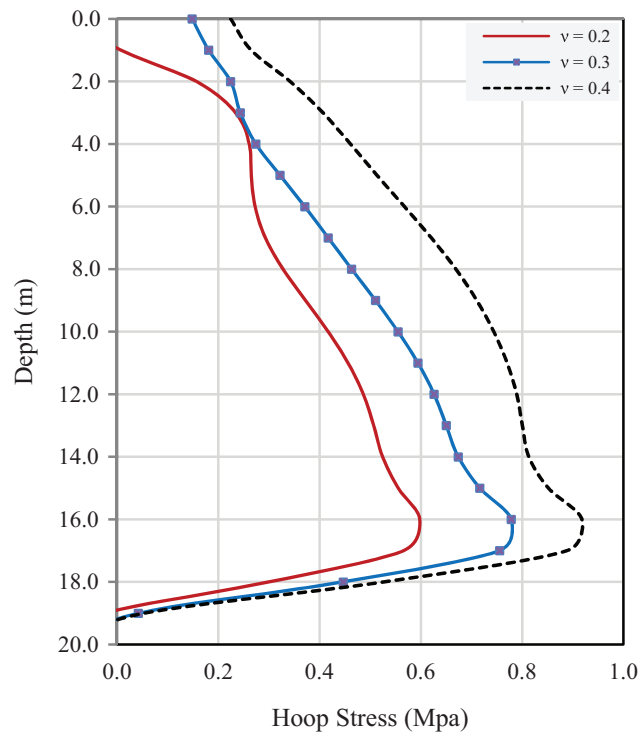


Figure 23: The effect of stored material Poisson's ratio (ν) on the seismic hoop stress of the FE model

6.3 The Angle of Internal Friction

The internal friction angle (ϕ) of the stored material is one of the parameters that have been adopted in the Drucker-Prager model and the classic theories of describing the behavior of the material in the static and dynamic phases. The significance of that parameter can be observed in the plastification phenomenon of the stored material. Accordingly, lower values of the internal friction angle are expected to ease the plastification process in the stored material; which leads to producing higher lateral pressure. Hence, this claim has been proven by examining various values of ϕ to determine its influence on the dynamic hoop stress of silo walls. The results have recorded a 36.2% increase in the maximum dynamic hoop stress when the internal friction angle is reduced from 60° to 20° .

6.4 The Dilation Angle

The dilation angle (ψ) is one of the components that characterize the behavior of granular material of an elastic-plastic type. So, it defines the volumetric change of a particulate material when it suffers shearing. The

value of the dilation angle may vary from zero up to the angle of internal friction (ϕ). However, testing different values of ψ has deduced that the dilation angle has a modest influence on the yielded dynamic hoop stress of about 2% growth when ψ was changed from 10° to 50° .

7 Summary and Conclusions

This study aims to numerically examine the dynamic seismic behavior of cylindrical flat-bottomed reinforced concrete silos, taking into account the influence of near-fault and far-field ground motions. The concrete damage plasticity was utilized for the silo wall and the granular material was represented by the Drucker-Prager plastic model. In addition, the interaction between the silo wall and ensiled material was introduced by Coulomb's constant friction theory; permitting material separation and local loss of contact. The proposed model was verified with experimental data and theoretical expressions. However, the impact of slenderness ratio (S_r) was incorporated by examining four slenderness ratios of $S_r = 1.0$, $S_r = 2.0$, $S_r = 3.0$, and $S_r = 4.0$. The main conclusions of this study are as follows:

1. There is a remarkable difference in the seismic response of the RC silos under NFGM and FFGM in terms of stresses, base shear, overturning moments, and concrete damage propagation. This conclusion is valid for all the four studied models under earthquakes with an identical PGA. Hence, the time profile of ground motions plays a significant role in the seismic behavior of silos.
2. The slenderness ratio (S_r) of RC silos has a direct impact on the behavior of silos under seismic loading. However, the seismic responses to NFGM and FFGM have fluctuated over various slenderness ratios.
3. Squat silos ($S_r \leq 1.0$) have unique seismic performance compared to slender silos. For instance, the FFGM dominates the seismic behavior of squat silos, and their distribution of wall stresses produces perfectly compressive vertical stresses and plain tensile hoop stresses for both NFGM and FFGM.
4. Slender silos tend to endure larger seismic structural demand undergoing NFGM. However, the growth in the demand is not consistent with the increment of the slenderness ratio. Thus, the NFGM is found to impose spectacular seismic demand for the slender silo of $S_r = 3.0$ in respect of base shear, overturning moments, and wall stresses. Moreover, the distribution of the hoop stresses in slender silos has recorded an inflection depth in which the hoop stress inverted from tensile to compressive at the upper part of the silo. The difference in the distribution of stresses between the squat and slender silos is attributed to the effect of granular material packing pheromone which is a characteristic of wall-granular material interaction. Despite the influence of the material interaction in the seismic behavior of silos, the Eurocode-8 does not account for it in the calculations.
5. The position of the maximum hoop and vertical stresses is found to be near the base of the silo for the FFGM; whereas, the maximum hoop stresses of the NFGM are located closer to the middle part of the silo depth. Hence it is suggested to assign the max hoop steel reinforcement for the entire depth in the seismic design of RC silos.
6. The overall concrete damage propagation is more aggressive in the RC silo walls exposed to NFGM than those subjected to FFGM. Silos subjected to NFGM suffer concrete tension damage in high values of slenderness ratios ($S_r = 3$ and $S_r = 4$); meanwhile, there is no damage has occurred at low slenderness ratios ($S_r = 2$ and $S_r = 2$). However, the FFGM cause tension damage for a single case of $S_r = 3$, while all other models were free of damage. In terms of concrete compression crush, the slenderness ratio of $S_r = 3.0$ under NFGM is the only case that was found to have such failure. These conclusions illustrate two facts about the seismic behavior of RC silos; the first one suggests the tensile stress as the critical stress since it is the primary cause of concrete wall failures. Secondly, high-grade concrete is recommended in the seismic design of silos under

NFGM to avoid immediate structural collapse and to ensure the satisfaction of the secondary compression failure concept.

7. The Eurocode-8 part-4 provisions are adequate to control the seismic response of RC silos under FFGM and less effective in the NFGM. This behaviour under NFGM is particularly valid for slender silos of $S_r \geq 3.0$. The explanation of the Eurocode-8 being less effective with the NFGM can be assigned to two main reasons; firstly, the Eurocode-8 provides an alike procedure for silos of different slenderness ratios. Secondly, the interaction between the silo wall and the stored material is not considered in the Eurocode.
8. The selection of the granular material properties has an enormous impact on the dynamic stresses of silos. Poisson's ratio (ν), the wall-granular material friction coefficient (μ), and the angle of internal friction (ϕ) are the major parameters in the seismic response of reinforced concrete silos.

Funding Statement: The authors received no specific funding for this study.

Conflicts of Interest: The authors declare that they have no conflicts of interest to report regarding the present study.

References

1. Djelloul, Z., Mohammed, D. (2018). Contribution to the seismic behavior of steel silos: Full finite-element analysis versus the eurocode approach. *Asian Journal of Civil Engineering*, 19(7), 757–773. DOI 10.1007/s42107-018-0062-z.
2. Chavez Sagarnaga, J., Kulkarni, A. D. (2020). The need for a comprehensive standard/code for the design of bins and silos in the USA. *Structures Congress*, pp. 349–360. DOI 10.1061/9780784482230.034.
3. Matthias, M. C. (2020). Concrete silos: Failures, design issues and repair/strengthening methods. *Applied Sciences*, 10, 663–695 DOI 10.3390/app10113938.
4. Mahamid, M., Gaylord, H., Gaylord, C. (2020). *Structural engineering handbook*, Fifth Edition. NY, USA: McGraw Hill.
5. Eurocode-8 (2006). Design of structures for earthquake resistance—Part 4: Silos, tanks, and pipelines. European Committee for Standardization, rue de Stassart-36, B-1050 Brussels.
6. ACI 313-16 (2016). Design Specification for Concrete Silos and Stacking Tubes for Storing Granular Materials (ACI 313-16) and Commentary. American Concrete Institute, Farmington Hills, MI, USA.
7. Durmuş Demir, A., Livaoğlu, R. (2019). The role of slenderness on the seismic behavior of ground-supported cylindrical silos. *Advances in Concrete Construction*, 7, 65–74. DOI 10.12989/acc.2019.7.2.065.
8. Butenweg, C., Rosin, J., Holler, S. (2017). Analysis of cylindrical granular material silos under seismic excitation. *Buildings*, 7, 61. DOI 10.3390/buildings7030061.
9. Saleem, M., Khurshid, H., Qureshi, H., Siddiqi, Z. (2018). A simplified approach for analysis and design of reinforced concrete circular silos and bunkers. *The Open Construction and Building Technology Journal*, 12, 234–250. DOI 10.2174/1874836801812010234.
10. Silvestri, S., Ivorra, S., Chiacchio, L. D., Trombetti, T., Foti, D. et al. (2016). Shaking-table tests of flat-bottom circular silos containing grain-like material. *Earthquake Engineering & Structural Dynamics*, 45(1), 69–89. DOI 10.1002/eqe.2617.
11. Abd el-Rahim, H. H. A. (2013). Response of cylindrical elevated wheat storage silos to seismic loading. *JES. Journal of Engineering Sciences*, 41(6), 2079–2102. DOI 10.21608/jesaun.2013.114948.
12. Benkhellat, S., Kada, O., Seghir, A., Kadri, M. (2021). Seismic damage assessment of reinforced concrete grain silos. *International Journal of Structural Stability and Dynamics*, 22(1), 2250005. DOI 10.1142/S0219455422500055.
13. El-Arab, I. E. (2014). Seismic analysis of RC silos dynamic discharge phenomena. *International Journal of Engineering and Advanced Technology*, 4, 91–99.

14. Livaoglu, R., Durmuş, A. (2015). Investigation of wall flexibility effects on seismic behavior of cylindrical silos. *Structural Engineering and Mechanics*, 53, 159–172. DOI 10.12989/sem.2015.53.1.159.
15. Mansour, S., Pieraccini, L., Palermo, M., Foti, D., Gasparini, G. et al. (2022). Comprehensive review on the dynamic and seismic behavior of flat-bottom cylindrical silos filled with granular material. *Frontiers in Built Environment*, 7, 805014. DOI 10.3389/fbuil.2021.805014.
16. Maraveas, C. (2020). Concrete silos: Failures, design issues and repair/strengthening methods. *Applied Sciences*, 10(11), 3938. DOI 10.3390/app10113938.
17. Xu, Q., Zhang, H., Liu, Q., Wang, L. (2021). Seismic analysis on reinforced concrete group silos through shaking table tests. *Structural Concrete*, 22(3), 1285–1296. DOI 10.1002/suco.202000207.
18. Jouneghani, K., Hosseini, M., Rohanimanesh, M., Raissi Dehkordi, M. (2017). Evaluating main parameters effects of near-field earthquakes on the behavior of concrete structures with moment frame system. *Advances in Science and Technology Research Journal*, 11, 10–23. DOI 10.12913/22998624/74135.
19. Zhou, J., Sun, C., Dai, X., Chen, G. (2019). Seismic reliability assessment of inelastic SDOF systems subjected to near-fault ground motions considering pulse occurrence. *Structural Durability & Health Monitoring*, 13(4), 361–378. DOI 10.32604/sdhm.2019.05171.
20. Sgobba, S., Lanzano, G., Pacor, F., Felicetta, C. (2021). An empirical model to account for spectral amplification of pulse-like ground motion records. *Geosciences*, 11(1), 15. DOI 10.3390/geosciences11010015.
21. Bray, J. D., Rodriguez-Marek, A. (2004). Characterization of forward-directivity ground motions in the near-fault region. *Soil Dynamics and Earthquake Engineering*, 24(11), 815–828. DOI 10.1016/j.soildyn.2004.05.001.
22. Zhao, D., Wang, H., Wang, D., Zhu, R., Zhang, J. (2022). Quantitative classification of near-fault ground motions selected by energy indicators. *Structures*, 35, 780–791. DOI 10.1016/j.istruc.2021.11.032.
23. Kohrangi, M., Vamvatsikos, D., Bazzurro, P. (2018). Pulse-like versus non-pulse-like ground motion records: Spectral shape comparisons and record selection strategies. *Earthquake Engineering & Structural Dynamics*, 48(1), 48–64. DOI 10.1002/eqe.3122.
24. Yang, J., Li, P., Jing, H., Gao, M. (2021). Near-fault ground motion influence on the seismic responses of a structure with viscous dampers considering SSI effect. *Advances in Civil Engineering*, 2021, 6649124. DOI 10.1155/2021/6649124.
25. Chang, T. Y., Cotton, F., Tsai, Y. B., Angelier, J. (2004). Quantification of hanging-wall effects on ground motion: Some insights from the 1999 Chi-chi earthquake. *Bulletin of the Seismological Society of America*, 94(6), 2186–2197. DOI 10.1785/0120030233.
26. Kalkan, E., Kunnath, S. K. (2006). Effects of fling step and forward directivity on seismic response of buildings. *Earthquake Spectra*, 22(2), 367–390. DOI 10.1193/1.2192560.
27. Dang, P., Cui, J., Liu, Q. (2022). Parameter estimation for predicting near-fault strong ground motion and its application to Lushan earthquake in China. *Soil Dynamics and Earthquake Engineering*, 156, 107223. DOI 10.1016/j.soildyn.2022.107223.
28. Eurocode-1 (2006). Actions on structures–Part 4: Silos and tanks. European Committee for Standardization, rue de Stassart-36, B-1050 Brussels.
29. Nguyen, Q. T., Livaoglu, R. (2020). The effect of the ratio of Λ -shaped shear connectors on the flexural behavior of a reinforced concrete frame. *Advances in Structural Engineering*, 23(12), 2724–2740. DOI 10.1177/1369433220920442.
30. Mehrehteran, A., Maleki, S. (2020). Evaluation of normal pressures during filling in steel hoppers with eccentric outlet. *Journal of Civil Engineering and Construction*, 9, 138–149. DOI 10.32732/jceec.2020.9.3.138.
31. Wang, Y., Lu, Y., Ooi, J. (2015). A numerical study of wall pressure and granular flow in a flat-bottomed silo. *Powder Technology*, 282, 43–54. DOI 10.1016/j.powtec.2015.01.078.